Atmos. Meas. Tech., 11, 1707–1723, 2018
https://doi.org/10.5194/amt-11-1707-2018

Atmospheric Measurement Techniques
Open Access
EGU

A new photometric ozone reference in the Huggins bands: the absolute ozone absorption cross section at the 325 nm HeCd laser wavelength

Christof Janssen[1], **Hadj Elandaloussi**[1], **and Julian Gröbner**[2]

[1]Sorbonne Université, Observatoire de Paris, Université PSL, CNRS, Laboratoire d'Etudes du Rayonnement et de la Matière en Astrophysique et Atmosphères, LERMA-IPSL, 75005 Paris, France
[2]Physikalisches Meteorologisches Observatorium Davos, World Radiation Center, Davos Dorf, Switzerland

Correspondence: Christof Janssen (christof.janssen@upmc.fr)

Received: 24 August 2017 – Discussion started: 4 October 2017
Revised: 19 January 2018 – Accepted: 23 January 2018 – Published: 27 March 2018

Abstract. The room temperature (294.09 K) absorption cross section of ozone at the 325 nm HeCd wavelength has been determined under careful consideration of possible biases. At the vacuum wavelength of 325.126 nm, thus in a region used by a variety of ozone remote sensing techniques, an absorption cross-section value of $\sigma = 16.470 \times 10^{-21}$ cm^2 was measured. The measurement provides the currently most accurate direct photometric absorption value of ozone in the UV with an expanded (coverage factor $k = 2$) standard uncertainty $u(\sigma) = 31 \times 10^{-24}$ cm^2, corresponding to a relative level of 2 ‰. The measurements are most compatible with a relative temperature coefficient $c_T = \sigma^{-1}\partial_T\sigma = 0.0031$ K^{-1} at 294 K. The cross section and its uncertainty value were obtained using generalised linear regression with correlated uncertainties. It will serve as a reference for ozone absorption spectra required for the long-term remote sensing of atmospheric ozone in the Huggins bands. The comparison with commonly used absorption cross-section data sets for remote sensing reveals a possible bias of about 2 %. This could partly explain a 4 % discrepancy between UV and IR remote sensing data and indicates that further studies will be required to reach the accuracy goal of 1 % in atmospheric reference spectra.

1 Introduction

High-resolution reference data for ozone absorption in the UV are widely called for, as this region is used for remote and in situ measurement of atmospheric ozone concentrations, and new measurements are therefore under way in the framework of the ESA TROPOMI/Sentinel 5 precursor mission that aims at establishing an improved atmospheric spectroscopy database (SEOM-IAS). The demands for augmented quality of these atmospheric measurements have been increasing continuously over the last decades in order to fulfil the requirement of reliably detecting small atmospheric changes. This was highlighted in the last report of the "Absorption Cross-Sections of Ozone" (ACSO, http://igaco-o3.fmi.fi/ACSO) from the joint initiative of the International Ozone Commission (IO3C), the World Meteorological Organisation (WMO) and the Integrated Global Atmospheric Chemistry Observations (IGACO) O_3/UV subgroup, which was dedicated to studying, evaluating and recommending the most suitable cross-section data to be used in atmospheric ozone measurements (Orphal et al., 2016). Remote sensing of tropospheric ozone by joint retrieval of UV and IR satellite instruments is another emerging application (e.g. Cuesta et al., 2013) that strongly depends on unbiased UV spectroscopic data as most of the ozone resides in the stratosphere, but accurate knowledge of the ozone spectrum is also required for the retrieval of other, less abundant trace gases that absorb in spectral ranges where ozone acts as an interfering species.

Reference cross-section values with an uncertainty of 1 % or better at the 90 % confidence level have only recently become available at and around the Hg line position of 253.65 nm (Viallon et al., 2015). This wavelength is particularly important, because absorption at this position is currently used as an ozone standard via standard reference photometers (Hearn, 1961; Viallon et al., 2006). At other wavelengths, such SI-traceable data at a similar accuracy level are not available, and currently used absorption cross-section data in the atmospheric remote sensing of ozone (GSWCB, BDM, BP which stand for Gorshelev, Serdyuchenko, Weber, Chehade and Burrows Gorshelev et al., 2014; Serdyuchenko et al., 2014, Brion, Daumont and Malicet, Brion et al., 1993; Daumont et al., 1992; Malicet et al., 1995, and Bass and Paur, Bass and Paur, 1985; Paur and Bass, 1985) do not provide the same level of accuracy and traceability, which might lead to inconsistent and biased results.

However, the UV range between 302 and 340 nm in the Huggins bands of ozone is particularly interesting for ozone column measurements from the ground using Brewer and Dobson spectrophotometers or for ozone retrieval using differential optical absorption spectroscopy with ground-based or satellite instruments. The traceability of total column ozone including a comprehensive uncertainty budget is thus an important objective of the Joint Research Project ATMOZ (traceability for ATMospheric total column OZone) within the European Metrology Research Programme (EMRP). The retrieval of total column ozone from solar radiation measurements in the Huggins band requires cross sections with very low uncertainties and well-defined temperature coefficients to take into account the effective ozone temperature which varies depending on location and season.

In this article we present new measurements of the UV absorption cross section at the HeCd laser wavelength using the photometric method. Particular attention has been paid to the pressure measurement, the sample purity and the decomposition of ozone during the measurement process. This has led to an improvement of a factor of about 10 in the overall uncertainty of the measurement when compared to the reference of Hearn. The measurement thus provides a new reference in the spectral region that is most important for atmospheric remote sensing of ozone. An uncertainty budget following the *ISO Guide to the Expression of Uncertainty in Measurement* (GUM) is given and instrumental biases that might have affected earlier measurements are discussed in detail.

2 Experimental setup and methodology

2.1 Ozone production and handling

Ozone is produced from high purity oxygen gas (99.9995 %, Air Liquide, France) in a dedicated vacuum system that has been described elsewhere (Janssen et al., 2011). Here we briefly describe some key points (see Fig. 1). The system is made from Pyrex and equipped with all glass valves using PTFE fittings. The only metal parts are gas flasks, pressure gauges, the turbo-molecular pump and stainless steel parts that connect these components. Ozone is produced by electric discharge at LN_2 temperatures in a 3 L reactor, to which copper electrodes are attached at the outside of the walls. After several evaporation and re-condensation cycles, the sample is transferred into a cold trap operating at 65 K, where it is further purified and then released into the absorption cell. The total volume of the cell, which can be closed off by an all-glass stopcock equipped with PTFE fittings, is 113 cm^3.

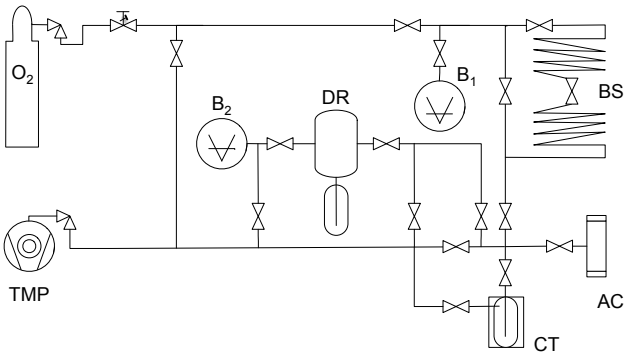

Figure 1. Vacuum system for ozone sample preparation. AC: UV absorption cell; B_1: Baratron 690 (10 Torr); B_2: capacitive pressure gauge (1000 hPa); BS: gas buffer spiral; CT: cold trap operable at 65 K; DR: electric discharge reactor chamber (3 L); and TMP: turbo-molecular pump.

2.1.1 Sample pressure

Over the last 3 years, the capacitive 10 Torr pressure head (Baratron 690, MKS) of high accuracy (0.08 % nominal) is regularly calibrated at 1-year intervals by the French National Metrology Institute (LNE; last certificate no. P156207/1). Due to metal surfaces in the gauge and the stabilisation at +45 °C, slight ozone decomposition has been observed. In order to improve the stability during the pressure reading, a buffer gas technique has been employed (Janssen et al., 2011).

2.1.2 Sample temperature

Four thin film four-wire Pt100 sensors were distributed over the length of the absorption cell and attached to its outside. The signals were registered continuously by a Picotech (pt-104) data logger. The probes and data logger were calibrated right after the measurement series by an in-house comparison with a traceable standard platinum reference thermometer (SPRT-5626, Hart Scientific) coupled to a readout unit (1502A, Hart Scientific). The calibration uncertainty ($k = 2$) of 14 mK is smaller than observed temperature gradients.

2.2 Photometer setup

The absorption measurements are performed using a custom-made photometer, of which an overview is given in Fig. 2. As a light source, a HeCd laser (Kimmon) is used. It delivers around 12 mW of output power at the laser wavelength of 325 nm. The laser light passes through a chopper, which modulates the beam amplitude at a frequency of about 2 kHz. The beam is then widened and only a small portion is selected by a ~ 1 mm pinhole. A 30 : 70 beam splitter divides the beam and projects the reflected part on the reference detector. The transmitted beam is guided twice through the 30 cm long absorption cell using a flat mirror at the backside of the cell. Both the signal (I) and the reference intensities (I_r) are measured using cooled Si photovoltaic detectors (Newport/Oriel) with integrated transimpedance preamplifiers. The cell windows have a vertical inclination of 3° with respect to the optical axis in order to avoid light being reflected back and forth between the two cell windows to fall onto the detectors. The amplitude modulation of the beam intensity allows for phase-sensitive detection of the reference and absorption signals, which are measured by digital lock-in amplifiers (SRS 830). Their output signals are registered by a PC using a multi-purpose data acquisition card (NI PCI-6281).

2.3 Sample purity and control measurements

In order to control and assess the purity of the ozone sample, a strict protocol of sample preparation, cell filling and pressure measurements has been followed, as described elsewhere (Janssen et al., 2011). After the measurement has been completed, the sample was re-condensed in a cold trap kept at a temperature of about 65 K. From the residual pressure, the mole fraction ν_{nc} of non-condensable impurities, such as air, that might have entered the system through small leaks, or oxygen that originates from ozone decomposition, could be estimated. The small mole fraction ν_c of condensable impurities that might be present in the current absorption cell has been estimated previously (Janssen et al., 2011). No attempt was made to repeat that quantification here. This was motivated by the fact that ozone decomposition rates in the absorption cell and the amount of non-condensable impurities after the experiment have not changed since. In the earlier study, the mole fractions of water, carbon dioxide, nitrous oxide and nitrate were measured and found to be $-0.10(17)$, $0.07(7)$, $0.3(3)$ and $-0.01(6)$ mmol mol^{-1} respectively. Moreover, an upper limit of all nitrogen containing impurities of 1.3 mmol mol^{-1} was found (Janssen et al., 2011, Table I).

2.4 Straight-line fit and data evaluation

The Beer–Lambert law implies a proportionality between the optical density τ and the absorbers' column density $\xi = n \cdot L$:

$$\tau = -\ln\left(\frac{(I/I_r)_m}{(I/I_r)_0}\right) = \sigma \cdot (n \cdot L) = \sigma\xi, \quad (1)$$

with the absorption cross-section σ being the proportionality constant. The I/I_r ratios designate intensities that are normalised for laser intensity fluctuations by means of a reference beam (I_r) and indices m and 0 indicate an ozone and an empty cell measurement respectively. In a plot of the optical density τ vs. ξ, the cross-section σ is obtained as the slope of this linear relation. Due to uncertainties in both variables, a standard least-squares fit is not appropriate. Because ozone column data are correlated (Bremser and Hässelbarth, 1998; Viallon et al., 2015), a weighted total least-squares (WTLS) fit with correlated uncertainties is required. The solution of the total least-squares problem ultimately goes back to Deming (1943), and there is now a wealth of literature on the York–Williamson algorithm which treats the straight-line adjustment with and without correlated uncertainties in x–y data pairs (York, 1966, 1968; Williamson, 1968; York et al., 2004; Reed, 2015, for example). The algorithm is frequently used in environmental, geochemical and isotope studies (e.g. York, 1968; Ludwig and Titterington, 1994; Cantrell, 2008; Wehr and Saleska, 2017). It seems, however, that fewer studies (e.g. Amiri-Simkooei et al., 2014; Bremser and Hässelbarth, 1998; Bremser et al., 2007; Malengo and Pennecchi, 2013) are devoted to the problem of when the structure of the covariance matrix is more complex and when correlations exist between uncertainties in different values of x and/or y. This type of question arises in chemometric or metrological applications when calibration lines need to be used or when instruments are to be compared.

In order to treat the latter problem, we use here an algorithm from Amiri-Simkooei et al. (2014), which we implement using the Mathematica software (Wolfram Research, Inc., 2016). Our implementation provides the fit coefficients a and b of the straight-line function $y = a\,x + b$, the associated standard uncertainties $u(a)$ and $u(b)$, Pearson's correlation coefficient $r(a, b)$ and the chi-squared value χ^2. The code has been tested on all benchmarks in the ISO technical specification (ISO, 2010, data given in Tables 4, 6, 10, 22 and 25 therein). These include the case of uncertainties in x and y, and the two cases when there are covariances associated with the y values and when covariances are associated with both x and y values. Our results agreed within all digits indicated. We also note that our implementation further matched all example calculations given in the original publication of Amiri-Simkooei et al. (2014). This comprises the classical data set from Pearson with York's weights assuming no correlations in x–y data pairs (York et al., 2004), but agreement to all digits as given by Reed (2015) is also obtained when such a correlation is considered.

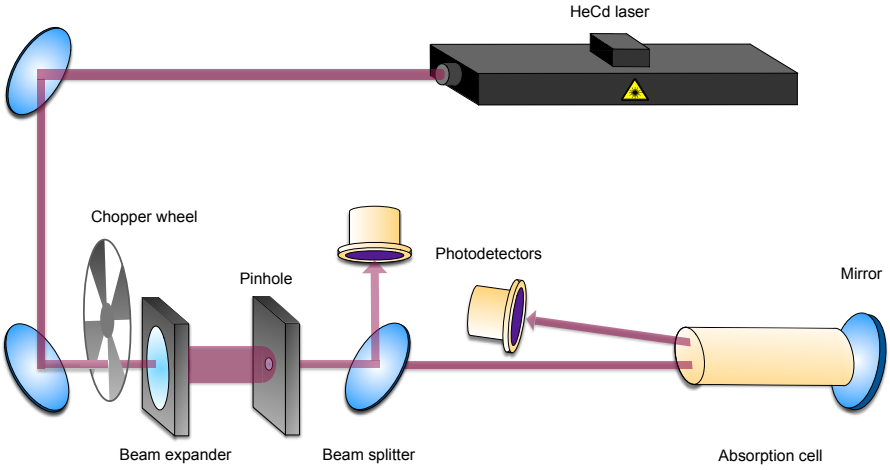

Figure 2. Scheme of the optical system. The beam of a HeCd laser is chopped, widened and directed through a pinhole before impinging on a beam splitter. The reflected beam provides the reference signal for the correction of laser intensity fluctuations. The transmitted beam passes through the absorption cell twice before being registered by a photodetector. Cell windows are slightly inclined with respect to the optical axis.

3 Analysis and uncertainty budget

3.1 Laser wavelength

We are not aware of direct interferometric measurements of the $4d^9 5s^2 : {}^2D_{3/2} \rightarrow 4d^{10} 5p : {}^2P^\circ{}_{1/2}$ laser transition at 325 nm. Reported wavelength values are based on the analysis of emission spectra of the Cd^+ ion produced in electric discharges. Previous atmospheric studies (Lakkala et al., 2008; Lantz et al., 2002) using a HeCd laser mostly report an air wavelength of 325.029 nm. This number emanates probably from term energies reported in the handbook of basic atomic spectroscopic data (Sansonetti and Martin, 2005) that are ultimately based on one comprehensive study (Shenstone and Pittenger, 1949). Other databases, reference tables and handbooks (e.g. Reader et al., 1980; Haynes, 2015) recommend the slightly different value of 325.033 nm, which corresponds to the wavelength that Shenstone and Pittenger (1949) actually measured for this transition. While the 0.004 nm difference between the measured and the term energy derived transition energy is compatible with the measurement uncertainty of $\sim 0.1\,\mathrm{cm}^{-1}$, Burns and Adams (1956) confirmed the Shenstone and Pittenger (1949) measured value at a much lower degree of uncertainty ($< 0.01\,\mathrm{cm}^{-1}$). Indeed, the more accurate of the two measurements resulted in a vacuum wavelength $\lambda_{\mathrm{vac}} = 325.126$ nm, which under standard conditions ($T = 15\,^\circ\mathrm{C}$, $p = 101\,325$ Pa) and reasonable variation of the air molecular composition ($\mathrm{RH} = (50 \pm 50)\,\%$ and $x(\mathrm{CO_2}) = (0.4 \pm 0.1)\,\mathrm{mmol\,mol}^{-1}$), corresponds to the air wavelength $\lambda_{\mathrm{air}} = 325.033$ nm with all figures significant to the last digit (Ciddor, 1996).

Further confidence into the claimed wavelength accuracy might be obtained by comparing measured and tabulated wavelengths of the well-studied HeNe laser. The Atomic Spectra Database gives an air wavelength of 632.8614 nm for the Ne I transition, corresponding to a vacuum wavelength $\lambda_{\mathrm{HeNe}} = 632.9914$ nm (when standard conventions are applied: $T = 15\,^\circ\mathrm{C}$, $p = 101\,325$ Pa, $x(\mathrm{CO_2}) = 0.33\,\mathrm{mmol\,mol}^{-1}$, $\mathrm{RH} = 0$). This result agrees to all digits with the reproducible line position of typical HeNe lasers (Mielenz et al., 1968).

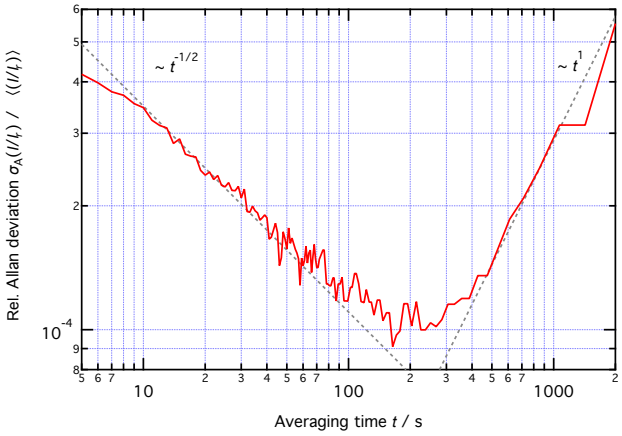

Figure 3. The stability of the photometer has been checked each measurement day after 2 h of laser warm up and before the measurements were performed. The measurement showing the lowest level of stability is shown. Data obtained on other days fall below the above curve, which is characterised by a white noise dependence ($\sim t^{-1/2}$) for about 100 to 180 s before a linear drift component becomes dominant.

3.2 Optical density

The stability of the laser fluctuation-corrected signal I/I_r is shown in Fig. 3. The displayed curve is characteristic for our system and allows for a conservative uncertainty estimation, because curves at other measurement days gave values at a lower level. We chose integration times of about 30 s for the ozone and empty cell measurements, which were taken within a time span of about 2 min. For the ratio $(I/I_r)_m / (I/I_r)_0$ we infer a measurement uncertainty of

$$u(\tau) = 1.8 \times 10^{-4} \sqrt{(3 + \exp(\tau))/2}, \quad (2)$$

where τ denotes the optical density of the absorption measurement. In deriving the above expression we assumed firstly that the measurements of the empty cell (0) and of the cell filled with ozone (O_3) are stochastically independent (white noise behaviour) during the whole measurement period that lasted for about 2 min, secondly that intensities of the empty cell and the reference beam contribute equally and thirdly that the relative uncertainty of the filled cell signal scales with $1/\sqrt{I_m} \sim \sqrt{\exp(\tau)}$. As the measurement signal is the ratio of two intensity ratios (thus the product/ratio of four measurement signals), the relative uncertainty must yield $\sqrt{2}$ times the 30 s level in Fig. 3 for $\tau = 0$. Note that the value of 2.1×10^{-4} in Fig. 3 is conservative, because the spectrometer stability at other days was always better. We thus replaced that number with the moderately lower and more representative value of 1.8×10^{-4}. For optical densities between 0.025 and 0.32, as in this study, Eq. (2) implies standard uncertainties $u(\tau)$ between 2.6×10^{-4} and 2.7×10^{-4}. This is only slightly higher than the residual scatter (2.5×10^{-4}) of our measurements (see Fig. 5b in Sect. 4.1). The uncertainties correspond to relative values of $u_r(\tau)$ in the 0.08 to 1.0 % range.

3.3 Temperature

A temperature gradient along the cell of about 100 mK was observed. In the absence of more accurate data, we determined the cell temperature as the average of the minimal and maximal temperature during a measurement (~ 30 s). Taking into account the uncertainty of the calibration (7 mK), the standard uncertainty was determined as

$$u^2(T) = (T_{max} - T_{min})^2/12 + (7\,\mathrm{mK})^2. \quad (3)$$

3.4 Pressure

The capacitive pressure sensor is regularly calibrated at LNE. The calibration determines the measurement uncertainty from the scatter of repeated readings and the standard uncertainty of the LNE working standard. In the relevant 10 Torr range, reading errors were shown to be negligible. However, there is a small pressure rise observed during the measurement, which is likely due to some ozone decomposition. This 0.04 Pa rise leads to an additional standard uncertainty of 0.01 Pa. Taken together with the calibration uncertainty we obtain

$$u(p) = 0.05\,\mathrm{Pa} + 10^{-3} p. \quad (4)$$

The laboratory temperature has an effect on offset and span of our sensor. While the offset is always readjusted, we need to consider the manufacturer-specified span temperature coefficient of $2 \times 10^{-5}\,\mathrm{K}^{-1}$. We are always within ± 2.5 K of the calibration temperature, which adds an uncertainty of 5×10^{-5} to the span. Because this is at least 20 times smaller than the calibration uncertainty, we can simply ignore it here. The dominant pressure uncertainties in Eq. (4) are of type B and do not lessen over repeated measurements. This is confirmed by the long-term drift between our sensor and the LNE working standard, which shows a characteristic pattern that evolves slowly over the calibration period of 3 years.

3.5 Optical path length

The path length was determined from the window thickness and calliper measurements of the outer cell dimensions combined with the observation of the entrance and exit positions on the two cell windows. A HeNe laser beam has temporarily been superposed to the UV beams and the cell centre axis in order to determine the different inclination angles. The procedure is described in detail in Appendix A. Altogether, seventeen different measurands contribute to the determination of the cell geometry and the orientation of the two beams with respect to the cell. All of these are included in the uncertainty budget of the optical path length $L = l_1 + l_2 = (596.654 \pm 0.243)$ mm (see Table 1), which is obtained as the sum of the individual lengths on the round trip through the cell. We only list and discuss the four factors that contribute most. The remaining non-listed quantities add less than 1 %.

The most important (95 %) contribution to the uncertainty is from the window thickness. The manufacturer-specified tolerance, which we verified on other windows of the same production batch, is ± 0.1 mm. We therefore deduce a standard uncertainty $u(d) = 100\,\mu\mathrm{m}/\sqrt{3} = 57.7\,\mu\mathrm{m}$. Superposing transparent millimetre paper on the cell windows allowed determination of the coordinates $(x_1, y_1, x_2, y_2$; see Appendix A) where the laser beams passed through the cell windows. A standard uncertainty of $u(y_1) = u(y_2) = u(x_1) = u(x_2) = 1\,\mathrm{mm}/\sqrt{3} = 577\,\mu\mathrm{m}$ is estimated for these measurements. They are listed at second and third position in Table 1. Since the cell is passed through by the laser beam 2 times, resulting in two beams with separate optical path lengths, these two contributions need to be accounted for twice. Due to the window inclination, the length is more sensitive to the vertical coordinate.

The forth most important contribution to the uncertainty is due to the shortest distance $\mathcal{L}$ between the inclined, but not exactly parallel windows. It was measured using a cal-

Table 1. Major contributions (> 99 %) to the standard uncertainty in the optical path length. Other factors contribute less than 1 %.

No.	Parameter	Probability distribution[a]	Value x/mm	Standard uncertainty $u(x)$/µm	Sensitivity coefficient $c(x)$	Contribution $\lvert c(x)u(x)\rvert$/µm
1.	Window thickness d	rect.	2.0	57.7	−4.008	231
2.	Beam[b] ordinate on entrance window y_1	rect.	−2	577	0.0601	35
3.	Beam[b] ordinate on exit window y_2	rect.	−3	577	−0.0598	35
4.	Shortest window distance[c] $\mathcal{L}$	gauss./rect.	301.77	10.2	2.003	20
	Optical path length L		596.654	243		

[a] rect.: rectangular; gauss.: Gaussian; [b] incident and reflected beam, which have the same y coordinates, contribute equally. Each entry must thus be accounted for twice.

liper that was compared to gauge block combinations with overall lengths of 290 and 300 mm. As the resolution of the calliper is 10 µm, the comparison with the gauge blocks always gave perfect agreement. The uncertainty of the length measurement was therefore obtained as the quadratic sum of two contributions: the standard uncertainty related to the calliper resolution ($5\,\mu m/\sqrt{3}$) and the error of the mean of eight measurements at two different days, which was found to be 9.8 µm.

The finite dimensions of the laser beam was also taken into account and found to be negligible compared to other factors. The beam divergence was estimated using the divergence angle $\alpha_d \sim 5 \times 10^{-4}$, determined from beam profile measurements before the entrance and after the exit of the cell. To first approximation, its effect ($\sim \sec(\alpha_d) - 1 \simeq \alpha_d^2/2 \simeq 10^{-7}$) on the path length is negligible. The finite diameter was explored through numerical simulations of parallel displacements of our beam centre. We shifted the centre by 1.5 mm (the beam diameter is between 2.6 and 3.3 mm) in all directions and found that the two displacements lead to changes of the length by less than 2 parts in 10^6.

3.6 Sample purity

The sample purity is characterised by the mole fractions of condensable (ν_c) and non-condensable gases (ν_{nc}). In a previous study, the mole fractions of CO_2, H_2O, N_2O, and NO_3 were determined and an upper limit for the sum of all oxides and hydrogen oxides of nitrogen, of $\nu_{nc} < 1.3\,\mathrm{mmol\,mol^{-1}}$ was found. Despite the fact that the observed mole fractions of the directly measurable quantities were all within one standard uncertainty or close to 0, we assume a rectangular probability distribution function (pdf) with bounds at 0 and $1.3\,\mathrm{mmol\,mol^{-1}}$. We thus obtain $\nu_{HxCyOz} = 0.65\,\mathrm{mmol\,mol^{-1}}$ with a standard uncertainty of $0.38\ \mathrm{mmol\,mol^{-1}}$. When combining this result with the observations on CO_2 and H_2O, we obtain $\nu_c = 0.62\,\mathrm{mmol\,mol^{-1}}$ with a standard uncertainty $u(\nu_c) = 0.42\ \mathrm{mmol\,mol^{-1}}$.

The mole fraction of non-condensables was determined from measurements of the residual pressure after condensation of the cell content as

$$\nu_{nc,max} = \gamma \cdot p_{res}/p, \tag{5}$$

where p_{res} is the residual gas pressure, and $\gamma = 7.24 \pm 0.44$ is a factor which takes into account the volume ratios and temperature gradients between the absorption cell, the volume where the residual pressure measurements are made and the cold finger where ozone is frozen back. The uncertainty of γ comprises the reproducibility of test measurements (1.9 %) and varying levels of LN_2 that change the effective volume of the cold finger (5.8 %). Residual pressure measurements are impacted by the thermal transpiration effect (Daudé et al., 2014) caused by the heating of the gauge (45 °C). It can be taken into account by assuming that the actual pressure is somewhere between the indicated value and the maximum of 4.2 % induced by thermal transpiration. This leads to a +2.1 % correction of the pressure reading with an associated standard uncertainty of the residual pressure measurement of 1.2 %.

The value in Eq. (5) is a limiting value, as it was obtained only after the measurement and it is likely that the non-condensables, in addition to entering into the measurement cell during sample admission, also get in especially when the re-condensation of ozone takes place and the residual pressures are measured. In the absence of further information, we simply assume a rectangular probability distribution $0 \leq \nu_{nc} \leq \nu_{nc,max}$ for each measurement. $\nu_{nc,max}$ varies between 1.3 and $4.8\,\mathrm{mmol\,mol^{-1}}$ with an average of $2.9\,\mathrm{mmol\,mol^{-1}}$. This amounts to a typical value of $\nu_{nc} = 1.4\,\mathrm{mmol\,mol^{-1}}$ with a standard uncertainty of $u(\nu_{nc}) = 0.84\,\mathrm{mmol\,mol^{-1}}$. We note that the dominating source of uncertainty comes from the unknown origin of the residual pressure and not from individual measurements.

3.7 Temperature dependence

For small variability, the temperature dependence of the absorption cross-section σ in the vicinity of some reference value σ_0 at $T = T_0$ is given by

$$\frac{\sigma(T)}{\sigma_0} - 1 = c_T(T - T_0), \tag{6}$$

where c_T is the normalised linear temperature coefficient. As shown further below, our measurements are most compatible with $c_T = 0.0031\,\mathrm{K}^{-1}$. This is close to data in the literature: $0.0033\,\mathrm{K}^{-1}$ (Serdyuchenko et al., 2014), $0.0042\,\mathrm{K}^{-1}$ (Malicet et al., 1995), and $0.0039\,\mathrm{K}^{-1}$ (Paur and Bass, 1985) at 325.03 nm and 294 K. Since the absorption cross section in the Huggins band is strongly wavelength and temperature dependent, we prefer using $c_T = 0.0031\,\mathrm{K}^{-1}$ as other values might be biased by small wavelength shifts. For the uncertainty estimate we assume a rectangular pdf with $0.0011\,\mathrm{K}^{-1}$ half width to obtain $u(c_T) = 0.00064\,\mathrm{K}^{-1}$.

3.8 Uncertainty budget for a single measurement

The uncertainty of a cross-section measurement is obtained from the Beer–Lambert law (Eq. 1), taking into account that the ozone column density ξ_i is given by

$$\xi_i = (n \cdot L)_i = \left(1 - \nu_\mathrm{c} - \nu_{\mathrm{nc},i}\right) L \frac{p_i}{k_\mathrm{B} T_i}, \tag{7}$$

where the different quantities have their previously defined meanings. However, as will become clear later, it is useful to define an adjusted ozone column density

$$\begin{aligned} x_i &= \xi_i \left(1 + c_T(T_i - T_0)\right) \\ &= \left(1 + c_T(T_i - T_0)\right) \left(1 - \nu_\mathrm{c} - \nu_{\mathrm{nc},i}\right) L \frac{p_i}{k_\mathrm{B} T_i}, \end{aligned} \tag{8}$$

where the slight temperature dependency of the absorption cross section is incorporated into the coordinate axis (see Sect. 4.1). Quantities with added index i vary between runs and must be determined for each individual ozone absorption measurement, while others, such as the path length L, always remain the same. These constants necessarily introduce a correlation between different values of x_i. For an individual measurement, where we ignore correlations and the temperature dependency of the cross section, simple error propagation rules yield the following equation for the relative uncertainty of the cross section

$$\begin{aligned} u_\mathrm{r}^2(\sigma) &= u_\mathrm{r}^2(\tau_i) + u_\mathrm{r}^2(\xi_i) \\ &= u_\mathrm{r}^2(\tau_i) + u_\mathrm{r}^2(k_\mathrm{B}) + u_\mathrm{r}^2(L) + u_\mathrm{r}^2(p_i) + u_\mathrm{r}^2(T_i) \\ &\quad + \frac{u^2(\nu_\mathrm{c}) + u^2(\nu_{\mathrm{nc},i})}{\left(1 - u(\nu_\mathrm{c}) - u(\nu_{\mathrm{nc},i})\right)^2}. \end{aligned} \tag{9}$$

The different contributions are summarised in Table 2 and a total relative standard uncertainty of $u_\mathrm{r}(\sigma) = 2.3 \times 10^{-3}$ is obtained for an individual measurement. This, for the moment, ignores the uncertainty caused by repeating measurements at slightly different temperatures, taken into account in the full analysis presented later in Sect. 4. The most prominent contributions ($> 1\,‰$) are due to the measurement of the optical density and the pressure. Repeated measurements will allow improvement in measurement uncertainty, provided that correlations in the pressure and other data contributing to the ozone column density are taken into account.

3.9 Correlations between realisations of the ozone column density

Equation (8) provides also the basis for the evaluation of measurement correlations. Constants in that equation clearly introduce a correlation between different values of x_i, but individual realisations of temperature, pressure and the mole fraction of non-condensable impurities are also not strictly independent from one run to another, because their measurements rely on the same calibrations and sensors. The correlation coefficients $r_{ij} = u^2(x_i, x_j)/(u(x_i)u(x_j))$ between two measurements i and j of the ozone column x can be calculated from Eq. (8), using correlations between the independent measurement quantities and a generalised error propagation rule. Details of the procedure are presented in Appendix B. We obtain

$$\begin{aligned} \frac{u^2(x_i, x_j)}{x_i x_j} &= u_\mathrm{r}^2(k_\mathrm{B}) + u_\mathrm{r}^2(L) \\ &\quad + \frac{(T_i - T_0)(T_j - T_0)u^2(c_T)}{(1 - c_T(T_i - T_0))(1 - c_T(T_j - T_0))} \\ &\quad + \frac{u^2(\nu_\mathrm{c}) + u^2(\nu_{\mathrm{nc},i}, \nu_{\mathrm{nc},j})}{(1 - \nu_\mathrm{c} - \nu_{\mathrm{nc},i})(1 - \nu_\mathrm{c} - \nu_{\mathrm{nc},j})} + \frac{u^2(p_i, p_j)}{p_i p_j} \\ &\quad + \frac{(1 - c_T T_0)^2}{(1 - c_T(T_i - T_0))(1 - c_T(T_j - T_0))} \frac{u^2(T_i, T_j)}{T_i T_j}, \end{aligned} \tag{10}$$

where k_B, L, ν_c and c_T are the independent quantities common to all determinations and where the variables p_i, T_i and $\nu_{\mathrm{nc},i}$ are newly determined in each run. The similarity with Eq. (9) is apparent. Indeed with the exception of the term for the optical density, we immediately recover Eq. (9) by setting $i = j$ and $u(c_T) = c_T = 0$. There is no uncertainty $u(T_0)$ associated with the arbitrarily chosen reference temperature T_0, which explains the absence of a corresponding term. The calculation of the different terms for $i \neq j$ is detailed in the remainder of this section.

The Boltzmann constant and the absorption path length contribute via their absolute or relative standard uncertainties to r_{ij}. We obtain (see Tables 2 and 3)

$$u_\mathrm{r}(x_i) u_\mathrm{r}(x_j) r_{ij}\big|_{k_\mathrm{B}, L} = 1.672 \times 10^{-7}. \tag{11}$$

Similarly, the contribution to the correlation coefficient through temperature variation of the absorption cross section is

$$u_\mathrm{r}(x_i) u_\mathrm{r}(x_j) r_{ij}\big|_{c_T} = \frac{4.033 \times 10^{-7}\,\mathrm{K}^{-2}(T_i - T_0)(T_j - T_0)}{(1 - c_T(T_i - T_0))(1 - c_T(T_j - T_0))}. \tag{12}$$

Table 2. Uncertainty budget of a single absorption cross-section measurement at average pressure

Parameter	Unit	Probability distribution[a]	Typical or recommended value X	Rel. standard uncertainty $u_r(X)$
Length L	mm	rect.	596.654	4.1×10^{-4}
Mole fraction complement of non-condensable impurities $(1-\nu_{nc})$	1	rect.	$1-1.4\times10^{-3}$	8.2×10^{-4}
Mole fraction complement of condensable impurities $(1-\nu_c)$	1	rect.	$1-6.2\times10^{-4}$	4.2×10^{-4}
Temperature T	K	gauss.	294.09	5.8×10^{-4}
Pressure p	hPa	gauss.	7.6	1.1×10^{-3}
Opt. density τ	1	gauss.	0.18	1.6×10^{-3}
Temperature dependence of cross section[b] c_T	K^{-1}	rect.	0.0031	2.1×10^{-1}
Boltzmann constant k_B	$J\,K^{-1}$	–	1.38064852×10^{-23}	5.7×10^{-7}
Cross-section σ	cm^2		16.47×10^{-21}	2.3×10^{-3}

[a] rect.: rectangular; gauss.: Gaussian; [b] contributes through additional weighting factor $\Delta T/T \sim 1.9\times10^{-3}$

Table 3. Contributions to correlation coefficients between different realisations x_i and x_j of the ozone column ($i \neq j$).

Quantity (y)	First-order contribution	Sensitivity coefficient $(\partial_y x_i)(\partial_y x_j)/(x_i x_j)$			r_{ij}	
		Average	Min	Max	Min	Max
Boltzmann constant k_B	$u_r^2(k_B)$	3.25×10^{-13}	–	–	–	–
Length L	$u_r^2(L)$	1.67×10^{-7}	–	–	–	–
Temperature coefficient c_T	$(T_i-T_0)(T_j-T_0)u^2(c_T)$	-4.79×10^{-9}	-5.00×10^{-7}	4.23×10^{-7}	–	–
Mole fraction ν_c of condensable impurities	$u^2(\nu_c)$	1.76×10^{-7}	1.76×10^{-7}	1.76×10^{-7}	–	–
Mole fraction $\nu_{nc,i}$ of non-condensables	$u(\nu_{nc,i},\nu_{nc,j})$	2.26×10^{-7}	5.01×10^{-8}	6.36×10^{-7}	–	–
Pressure p_i	$u(p_i,p_j)(p_i p_j)^{-1}$	4.70×10^{-8}	1.90×10^{-8}	2.89×10^{-7}	–	–
Temperature T_i	$u(T_i,T_j)(T_i T_j)^{-1}$	5.00×10^{-11}	5.00×10^{-11}	5.00×10^{-11}	–	–
Modified ozone column density x_i					0.76	1.00

As discussed in Sect. 3.8, individual measurements of non-condensable impurities ($\nu_{nc,i}$) are essentially fully correlated, which is due to the fact that it is not known whether the small amounts of residual gases have already been present during the measurement or were added only afterwards. We thus have $u^2(\nu_{nc,i},\nu_{nc,j}) = u(\nu_{nc,i})u(\nu_{nc,j})$ and, if we add the constant contribution from the condensables $u^2(\nu_c) = 1.764\times10^{-7}$, we obtain

$$u_r(x_i)u_r(x_j)r_{ij}\big|_{\nu_{nc},\nu_c} = \frac{0.577^2 u(\nu_{nc,i})u(\nu_{nc,j}) + 1.764\times10^{-7}}{(1-\nu_c-\nu_{nc,i})(1-\nu_c-\nu_{nc,j})}. \quad (13)$$

Temperature measurements are assumed to be non-correlated except for the contribution due to sensor calibration (7 mK):

$$u_r(x_i)u_r(x_j)r_{ij}\big|_T = \frac{49\times10^{-6}\,K^2(1-c_T T_0)^2}{(1-c_T(T_i-T_0))(1-c_T(T_j-T_0))T_i T_j}. \quad (14)$$

The uncertainty of the pressure measurement is essentially limited by the calibration. Repeated measurements at the same pressure will thus be fully correlated. Less is known about the correlation of measurements at different pressures. As pointed out by Viallon et al. (2015), assuming a high degree of correlation does not alter the derived value of the absorption cross section, but leads to a conservative uncertainty estimate. Therefore we assume full correlation $u^2(p_i,p_j) = u(p_i)u(p_j)$:

$$u_r(x_i)u_r(x_j)r_{ij}\big|_p = u_r(p_i)u_r(p_j). \quad (15)$$

The range of values for the different contributions is indicated in Table 3. Taking all parts together one gets hold of the correlation coefficient r_{ij}. Evidently, $r_{ij} = 1$ for $i = j$, but we still find an average value of $\overline{r_{ij}} = 0.94$ for $i \neq j$, indicating a very strong correlation between different measurements of the ozone column density. Most of this is due to the foreign gas contamination and the optical path length.

4 Analysis and results

Figure 4 shows the results of 27 individual measurements and an unweighted linear fit to the data. The measurements span the range of τ between 0.025 and 0.32, corresponding to ozone columns from 0.15 to 1.95×10^{19} cm^{-2}. A high coefficient of determination ($r^2 = 0.999977$) attests to the excellent linearity between optical densities τ and ozone columns ξ. Before the cross-section value can be derived, the impact

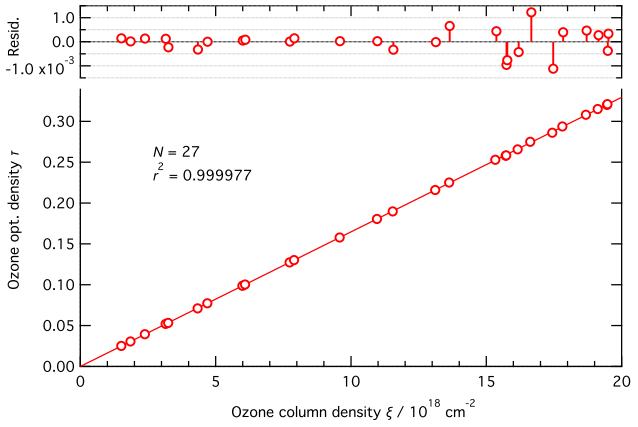

Figure 4. Unweighted linear fit to 27 individual pairs of ozone optical (τ) and column ($\xi = n \cdot L$) densities.

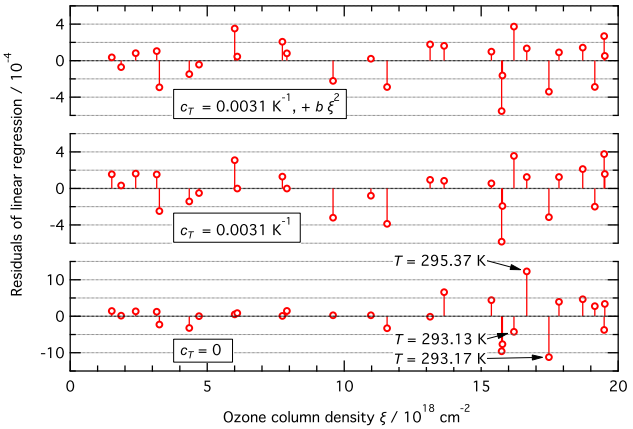

Figure 5. Study of residuals in the fitting of the absorption data using different variants of Eq. (17) as fitting functions. From bottom to top, the number of free fit parameters increases. The result of a simple linear fit ignoring the temperature dependence of the absorption cross section ($c_T = 0$ in Eq. 17) is shown on the bottom. Residual values with highest and the two lowest sample temperatures are indicated. The same fit including a temperature dependence ($c_T = 0.0031\,\mathrm{K}^{-1}$) is displayed on the middle panel. The top panel shows residuals when the fit includes an additional quadratic term ($+b\xi^2$) in the ozone column density. Scales in the two upper graphs are enlarged by a factor of 2.5.

of temperature and the choice of the fitting model need to be examined.

4.1 Preliminary analysis and choice of fitting function

As discussed previously, the data were obtained for temperatures varying slightly in the range between 293.17 and 295.37 K. This leads to some scatter due to the temperature dependence of the absorption cross section. Using a local linear dependency on temperature, the optical density will be given by

$$\tau(\xi, T) = \sigma(T)\xi = \sigma_0[1 + c_T(T - T_0)]\xi = \sigma_0 x(T), \quad (16)$$

where we defined the new variable $x = [1 + c_T(T - T_0)]\xi$ (see Eq. 8). In order to determine the cross section at the average temperature T_0, we can now plot τ vs. x, which directly yields the cross section σ_0 as the slope term. While we allow for an offset a in the linear fit that serves as an additional control, we also need to explore the possibility of non-linearities in our measurement chain, possibly caused by a saturation of the detectors or by other effects in the electronic acquisition and amplification modules. This can be accomplished by including a quadratic term ($b\xi^2$) in the fit, leading to the following fitting function:

$$\tau(\xi) = a + \sigma_0[1 + c_T(T - T_0)]\xi + b\xi^2. \quad (17)$$

Figure 5 shows the residuals of fitting this function for different scenarios. In the lower panel relatively large residuals with a reduced standard deviation (SD) of $S_\mathrm{r} = S \cdot \sqrt{27/25} = 5.0 \times 10^{-4}$ and prominent features at $\xi \sim 1.7 \times 10^{19}\,\mathrm{cm}^{-2}$ are observed, when we assume $b = c_T = 0$. Interestingly, the most variable temperature conditions (between -0.92 and $+1.28$ K with respect to the average) prevailed during measurements at these column densities. When a first-order correction $c_T = 0.0031\,\mathrm{K}^{-1}$ for the temperature is taken into account, the largest residual features disappear (as shown in the middle panel of Fig. 5) and the spread of residuals (max–min) is reduced by a factor of 2.0. Correspondingly, the reduced SD of the temperature-corrected residuals in the middle panel of Fig. 5 of $S_\mathrm{r} = S \cdot \sqrt{27/24} = 2.5 \times 10^{-4}$ is only half of that in the lower panel. It has to be noted that this number is only slightly lower than the standard uncertainty of the optical density τ, derived in Sect. 3.2.

Allowing for a quadratic term $+b\xi^2$ in the fit affects residuals (shown on the top panel of Fig. 5) only marginally, diminishing the reduced SD just by 3 % to yield $S_\mathrm{r} = 2.4 \times 10^{-4}$. At the same time, the quadratic term introduces a strong anti-correlation between fit parameters ($r(\sigma_0, b) = -0.98$). This indicates that, while the effect of temperature on the fit is well significant, quadratic terms are not. Our restriction to a straight-line fit is thus well justified in what follows. We also fix the temperature coefficient to our best fit value of $c_T = 0.0031\,\mathrm{K}^{-1}$, because the value is consistent with previously observed data (see Sect. 3.7) and because reasonable changes to this parameter do not modify our result significantly (see Sect. 4.2).

4.2 Linear regression

After having established the fitting function, the data are evaluated using the weighted total least-squares algorithm with correlated x–τ data. Table 4 summarises the results of the analysis.

Table 4. Linear fit statistics including standard uncertainty ($k = 1$) values.

Quantity	Unit	Value
Degrees of freedom ν	1	25
Slope σ	$10^{-20}\,\mathrm{cm}^2$	1.64704
Offset τ_0	1	6.684×10^{-6}
Slope uncertainty $u(\sigma)$	$10^{-23}\,\mathrm{cm}^2$	1.530
Offset uncertainty $u(\tau_0)$	1	1.033×10^{-4}
Pearson's coefficient $r(\sigma, \tau_0)$	1	−0.4092
Chi-squared χ^2	1	20.8469

The cross-section $\sigma_0 = 1.6470 \times 10^{-20}\,\mathrm{cm}^2$ with a relative standard uncertainty $u_\mathrm{r}(\sigma) = 9.3 \times 10^{-4}$ ($k = 1$) is obtained. The small offset within the uncertainty range indicates that the data comply with our hypothesis of a straight-line passing through the origin, and thus that our measurement follows the Beer–Lambert law. The χ^2 value falls within the 10 and 90 % quantiles of the cumulative χ^2_{25} distribution, which also indicates that the straight-line hypothesis does not need to be rejected and that the uncertainty analysis is compatible with our data.

The importance of considering covariances in this type of photometric absorption measurements (Bremser et al., 2007) is once more emphasised by comparing our results with numbers obtained when these covariances are omitted. Ignoring covariances firstly leads to an unrealistically small value of χ^2_{25} (12.6 instead of 20.8) and, secondly, underestimates $u(\sigma)$ by 34 %. However, the absolute value of σ is remarkably robust against ignoring the covariance terms (it changes only by 0.011 % if these are ignored). This finding is in line with the discussion of Viallon et al. (2015), where an effectively constant correlation coefficient $r = r_{ij}$ for all x_i-x_j pairs ($i \neq j$) was assumed. But we suspect that this might not generally be true. In particular if r_{ij} strongly varies as a function of i and j, we expect that the value of the cross section changes as well upon considering covariances. A possible scenario would be a measurement where different pressure sensors are utilised in different pressure ranges, possibly leading to little correlation between low- and high-pressure values, while maintaining a high correlation coefficient between measurements using the same gauge. We also note that the result is de facto independent of our choice of c_T. Using one of the highest values reported in the literature so far ($c_T = 0.0042\,\mathrm{K}^{-1}$ (Paur and Bass, 1985) instead of $c_T = 0.0031\,\mathrm{K}^{-1}$), the derived cross-section value changes by less than 1 part in 10^5 and the uncertainty estimate is not at all affected.

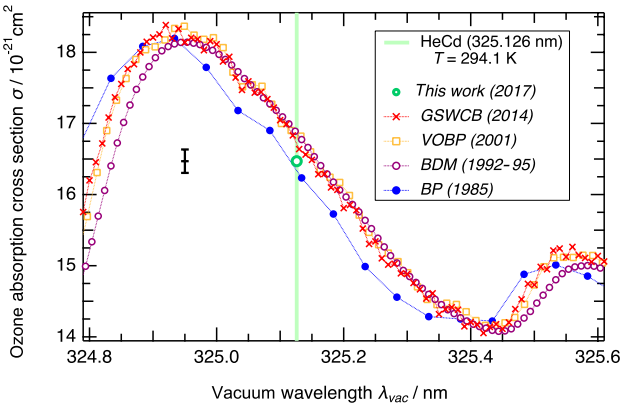

Figure 6. Comparison of high-resolution ozone absorption data around the 325 nm HeCd laser line (position indicated by vertical bar). The vacuum wavelength is used on the ordinate scale. Data are from the same sources as in Table 5. Straight lines between measurement points were inserted for visual guidance. Individual uncertainty bars have been omitted from the graph. The uncertainties of this work are smaller than the symbol size. Uncertainty assignments for other spectra are given in Table 5. As a reference, the black vertical bar indicates the ±1 % relative uncertainty range at $1.647 \times 10^{-20}\,\mathrm{cm}^2$.

5 Discussion

5.1 Comparison with laboratory data

Table 5 compares our result with previously published high-resolution data or cross sections commonly used for atmospheric retrieval. For convenience, the Table shows not only an analysis of the original data; it also includes the recent parametrisation of cross-section data from BP, BDM and GSWCB, and their uncertainties provided by Weber et al. (2016). Their investigation agrees well (better than 0.2 %) with our analysis of the original data when cross sections are smoothed. Interestingly, all of the literature data only insignificantly deviate from our reference measurement. Except for BP, the literature data sets agree well with each other at 325 nm, but they show values about 2 % higher than our measurement, independent of whether they were calibrated at the Hearn (1961) value (VOPB) or not (GSWCB, BDM). This is different from the situation around the top of the Hartley band. In that region Viallon et al. (2015) observed that data can be divided into two distinct groups: one where values are scaled to the absolute absorption cross section of Hearn, including the old Bremen (VOPB) data, and one where the absolute scale is determined independently, such as their own measurements, the new Bremen (GSWCB) and the Reims (BDM) data, the former group giving values about 2 to 3 % higher than the latter. Obviously this is not the case at the HeCd laser wavelength (see Table 5 and Fig. 6).

The negative offset of the BP data must mostly be explained by a wavelength bias (see Fig. 6). Early evaluations

Table 5. Comparison of absolute high-resolution absorption cross-section data of ozone at 325.126 nm in vacuum (325.033 nm in air). Smoothed data were obtained from applying a Savitzky–Golay filter of order 2 over the range of 0.1 nm.

Data set[a]	Temperature[b]	Cross-section σ (10^{-21} cm^2)			Rel. standard uncertainty[c] $u_r(\sigma)$ (%)		Relative deviation[d]
	(K)	original	smoothed	Weber et al. (2016)	from paper	Weber et al. (2016)	from this work (%)
BP (1985)	294.1	16.335	16.335	16.315	2.3	2.31	−0.8/0.7…2.5
BDM (1995)	294.1	16.864	16.863	16.896	2–4	1.74	2.4
VOPB (2001)	294.1	16.855	16.819	–	4–7	–	2.1
GSWCB(2014)	294.1	16.716	16.740	16.735	1.1–3	1.65	1.6
This work	294.09	16.470	–	–	0.093		

[a] Data were obtained from the ACSO website: http://igaco-o3.fmi.fi/ACSO/cross_sections.html. References are BP: Bass and Paur (1985), Paur and Bass (1985); BDM: Daumont et al. (1992), Malicet et al., 1995; VOPB: Voigt et al. (2001); and GSWCB: Gorshelev et al. (2014), Serdyuchenko et al. (2014) [b] The temperature dependence of the literature data has been taken into account using a quadratic parametrisation $\sigma(t) = \sigma_0(1 + c_1 t + c_2 t^2)$, where $t = T - 273.15$ K. BP and GSWCB provided corresponding coefficients σ_0, c_1 and c_2. For BDM and VOPB, these were obtained from a quadratic fit to cross sections given at fixed temperatures. [c] The uncertainty estimation of BDM contains the effect of wavelength shifts, not considered by BP, GSWCB and VOPB. [d] Based on smoothed data. BP cross sections suffer from wavelength bias: neg. value uncorrected; range of pos. values after correction (see text).

report shifts of the BP cross sections between 0.025 and 0.05 nm (Malicet et al., 1985, 1995; Orphal, 2003), and the existence of this bias is confirmed by comparison with atmospheric spectra (Orphal et al., 2016). When compared to atmospheric spectra, the BDM data, however, do not require any shift. In calculating differential cross sections (Platt and Perner, 1984) in the 320 to 330 nm range, we determine shifts of 0.049 nm between BP and BDM and 0.23 nm between BP and GSWCB. In combination with the strong wavelength dependency in the Huggins band (Fig. 6), which is quite different from the peak of the Hartley band that essentially is a spectrally flat region, the wavelength shift leads to a systematic bias in the cross-section value. Using a linear variation of the cross section of $\partial\sigma/\partial\lambda = -1.1 \times 10^{-20}$ cm^2 nm^{-1} (at 325.1 nm), common to all wavelength-dependent measurements in Fig. 6, would result in the BP cross section at the reference wavelength actually being higher than our measurement by 0.7 to 2.5 % (assuming the BP wavelength bias to be somewhere between 0.023 and 0.049 nm), thus implying a similar cross-section offset to the other data sets (see Table 5).

Despite the nominal agreement of our determination with all other measurements listed in Table 5, a concern might be the fact that all of these take higher values (when wavelength shifts are corrected for). It must therefore be pointed out that the study of Hearn (1961) gives values that are consistently lower than BDM and GSWCB by 2.7 to 3.7 % at three Hg line wavelength positions (289.4–302.2 nm) in the region around 300 nm. Furthermore, neither GSWCB nor BDM mention any particular precaution against multiple reflections in their optical setups. The presence of such reflections within the absorption cell leads to an overestimation of the absorption cross section (Viallon et al., 2006). Under the specified conditions, we estimate that a corresponding bias between +0.3 and +1.2 % for the GSWCB data or between +0.3 and +0.8 % for the BDM cross section could exist.

5.2 Atmospheric implications

The discrepancy at the HeCd laser wavelength indicates a 2 % room temperature bias in current atmospheric reference spectra used by a variety of remote sensing platforms and techniques (Brewer, Dobson, lidar, Umkehr, SBUV, TOMS, OMI, SCIAMACHY and GOME(-2); see Orphal et al., 2016, for example). If that bias applies to a larger wavelength region ($\sim$ 310–340 nm) and to most of the atmospheric temperature range, actual retrievals in this spectral region systematically underestimate atmospheric ozone by about 2 %. Although identical in magnitude this tentative bias in the Huggins bands is different from the ongoing discussion of whether the reference absorption cross section of Hearn (1961) at the Hg line position of 253.65 nm in the Hartley band should be reduced by about 2 % (Viallon et al., 2015; Orphal et al., 2016), because both the GSWCB and the BDM data are already compatible with the lower value at 253.65 nm, and only the BP data set, which is no longer recommended for atmospheric retrieval (Orphal et al., 2016), would be affected by the revision of the absorption cross section at 253.65 nm.

There is a long-standing consistency problem of atmospheric ozone derived from remote sensing in UV and IR spectral regions (e.g. Barbe et al., 2013; Janssen et al., 2016). Both laboratory (Picquet-Varrault et al., 2005; Gratien et al., 2010; Guinet et al., 2010) and atmospheric (Kagawa et al., 2007; Viatte et al., 2011) studies imply that using recommended spectroscopic data in the UV (BP/BDM) and IR (HITRAN2012 Rothman et al., 2013) leads to results that disagree by about 4 to 5 %, with ozone abundances inferred from IR measurements being higher. Thus when comparing measured (msd) and database (db) IR intensities (I) with UV cross sections (σ) through the ratio

$$\widetilde{R} = (I/\sigma)_{\mathrm{msd}}/(I/\sigma)_{\mathrm{db}} = (\sigma_{\mathrm{db}}/\sigma_{\mathrm{msd}})\,(I_{\mathrm{msd}}/I_{\mathrm{db}})\,, \qquad (18)$$

the above studies indicate a value $\widetilde{R}$ around 1.04 or 1.05, whereas consistent data require $\widetilde{R} = 1$. Note that the factor

$(I/\sigma)_{\mathrm{msd}}$ in this equation is the ratio of two absorption signals, where factors except for the molecular parameters, such as the concentration or light path geometry, ideally cancel. Our new absorption cross section at 325 nm suggests that the currently used values of σ_{db} might be too high by about 2 % ($\sigma_{\mathrm{db}}/\sigma_{\mathrm{msd}} \sim 1.02$) which brings IR and UV results to within 2 or 3 % if this bias is taken into account. The remaining discrepancy is already close to most measurement uncertainties, but also agrees remarkably well with the value $I_{\mathrm{msd}}/I_{\mathrm{db}} - 1 = 2.5\,\%$ observed by Guinet et al. (2010), who investigated 15 intense lines at 8.8 µm in the ν_1 fundamental. This situation thus is similar to the spectral conditions in the atmospheric UV–IR comparison of Viatte et al. (2011) using Brewer and FTS instruments, their IR analysis being based on the ν_1-ν_3 region at 9.6 µm. The atmospheric comparison of Kagawa et al. (2007) between concentrations from TOMS (UV) and from ground-based FTS (IR) does not directly depend on the intensities in the ν_1 fundamental. But the fact that most atmospherically relevant ozone vibrational intensities in HITRAN directly depend on transition moments of the ν_1 and ν_3 fundamentals implies that IR intensities in the 3 µm region should be corrected by the same amount (Rothman et al., 2005; Flaud et al., 2003), implying that the discrepancy observed in their study is resolved at the same time.

The new ozone cross section at the HeCd laser wavelength thus not only provides the first reference value with subpercent accuracy for ozone spectra in the Huggins bands; it also supplies independent evidence for a shared contribution of IR and UV biases to the UV–IR consistency problem of atmospheric ozone. This is the first evidence directly based on a measurement in the Huggins band, i.e. in the same UV band that is actually utilised for the atmospheric (Kagawa et al., 2007; Viatte et al., 2011) and laboratory (Picquet-Varrault et al., 2005; Gratien et al., 2010) inter-comparisons. A previous laboratory study (Guinet et al., 2010) depended on UV measurements in the Hartley band. Further systematic temperature- and wavelength-dependent studies with high accuracy will be required to work out the possible bias in currently used atmospheric reference spectra (BDM, GSWCB and forthcoming data) and confirm our assertion with respect to the share of bias between UV and IR data in the spectroscopic databases.

6 Conclusions

Using a HeCd laser spectrophotometer we have obtained the currently most accurate measurement of an ozone absorption cross section in the Huggins bands, and in the spectral region used by a variety of remote sensing techniques and platforms. The cross-section $\sigma = (16.470 \pm 0.031) \times 10^{-21}\,\mathrm{cm}^2$ was found at $\lambda_{\mathrm{vac}} = 325.126$ nm, and a full uncertainty budget in accordance with the guide to expression of uncertainty in measurements (GUM) has been presented. The expanded ($k = 2$) relative uncertainty is at the 2 ‰ level and thus significantly more accurate than previous measurements and well below the current target of 1 % for atmospheric applications. This high-accuracy level has been made possible by the use of a special ozone production and handling system and an elaborate analysis of the light path in a cell with slightly non-parallel windows. The measurement, together with a recent study at several wavelengths (244–257 nm) in the Hartley band (Viallon et al., 2015), demonstrates that a sub-percent accuracy can now well be achieved in laboratory ozone absorption investigations and shows that the accuracy of atmospheric measurements can be improved significantly.

Our new reference value suggests that absorption spectra currently used for atmospheric remote sensing of ozone possibly need to be revised towards lower values in the Huggins bands by about 2 %. Such a revision would likely impact most ozone retrievals in the UV and would also reduce the $\sim$ 4 % UV–IR discrepancy reported in atmospheric and laboratory studies by a factor of 2. The remaining 2 to 3 % need to be attributed to a bias in the IR data, which is compatible with a previous independent IR study. The often cited target uncertainty of 1 % has obviously not yet been reached in atmospheric reference spectra. This implies that further studies are required. The possible bias in the atmospheric reference spectra is likely wavelength dependent because atmospheric reference spectra need to be acquired in spectral slices to be combined to cover the entire range from the UV to the NIR, which is a consequence of the 7 orders of magnitude in absorption between the Hartley and the Wulf bands. One would thus ideally make high-accuracy measurements at regular wavelength intervals (10 or 20 nm or so) in order to investigate this wavelength dependence. Unfortunately, this is not highly feasible due to the need for suitable laser sources at all these different wavelengths. In our next step, we propose extending the current measurements to selected UV and VIS wavelengths (particularly around 254, 325 and 633 nm, for example) using both gas and tuneable lasers, and including the whole temperature range down to 190 K. Thus, relevant reference points or even small regions for actual or new atmospheric reference spectra can be obtained. These can be used to calibrate existing and future cross-section data, assess their accuracy, identify wavelength shifts and assure traceability in limited wavelength regions.

Data availability. Raw data displayed in Fig. 4 are available from the corresponding author on request.

Appendix A: Path length in cell with non-parallel windows

Here we describe how the absorption path length in a cell with inclined (but not necessarily parallel) windows is obtained. The full analytic expression was derived using an algebraic software package (Mathematica) and our uncertainty analysis was based on this exact solution. Its analytical form is too clumsy to be fully reproduced here. We prefer to give the closed analytic solution for a cell with parallel windows, together with the first-order correction for slightly non-parallel windows.

The general situation with arbitrarily inclined window plates is illustrated in Fig. A1. In the laboratory system, we define the z axis along the centres of two parallel plates of thickness d and radius R, measured between the outer surfaces of the windows. The first centre is located at $z = 0$, and the second at $z = L_0$. x_1 and y_1 coordinates respectively designate axes in the vertical and horizontal directions in the laboratory frame (x_2 and y_2 are similarly defined at the origin of the second window). Because windows are assumed to be spherical, two Euler angles suffice to define the window inclination: β_1 for rotation around the y_1 axis, and α_1 for rotation around the newly obtained x_1' axis. The passage of the light beam is defined by the coordinates on the entrance $((x_1',\ y_1') = (a_1, b_1))$ and exit window $((x_2',\ y_2') = (a_2, b_2))$ surfaces. We define $\alpha = (\alpha_1 + \alpha_2)/2$ and $\beta = (\beta_1 + \beta_2)/2$ to be the average inclination angles, and $\Delta y = b_2 - b_1$ and $\Delta x = a_2 - a_1$ as the changes of the horizontal and vertical displacements of the window coordinates between the beams' exit and entrance. We can also characterise the degree of non-parallelism by introducing the angle differences $\Delta\alpha = (\alpha_2 - \alpha_1)/2$ and $\Delta\beta = (\beta_2 - \beta_1)/2$.

Let us first note that the window centre distance L_0 can be obtained from the shortest distance $\mathcal{L}$ between the two inclined plates, measured with a calliper where the two outside jaws are oriented along the y_1 and y_2 axes:

$$L_0 = \frac{1}{\cos(\alpha - \Delta\alpha)} \times \left(\mathcal{L}\cos^2\alpha + \mathcal{L}\sin(\alpha)\sin(\alpha - 2\Delta\alpha) + R\sin(2\Delta\alpha)\right). \tag{A1}$$

In deriving this formula we made the convenient but non-restricting assumption that $0 \le \alpha_1 \le \alpha_2 < \pi/2$. Assuming that windows are parallel ($\Delta\alpha = \Delta\beta = 0$), the length of a single pass is given by

$$l^{(0)} = l_p^{(0)}\mathcal{A}(\Delta x, \Delta y), \quad \text{where} \quad l_p^{(0)} = \frac{\mathcal{L}}{\cos\alpha}\left(1 - \frac{2d}{\mathcal{L}\cos\beta}\right) \tag{A2}$$

is the length of the beam propagating parallel to the z axis and where the correction term

$$\mathcal{A}(\Delta x, \Delta y) = \sqrt{1 + \cos^2\alpha\left[\left(\frac{\Delta x}{\mathcal{L}}\right)^2 + \left(\frac{\Delta y}{\mathcal{L}}\right)^2 - 2\frac{\Delta x}{\mathcal{L}}\sin\beta - 2\frac{\Delta y}{\mathcal{L}}\tan\alpha\right]} \tag{A3}$$

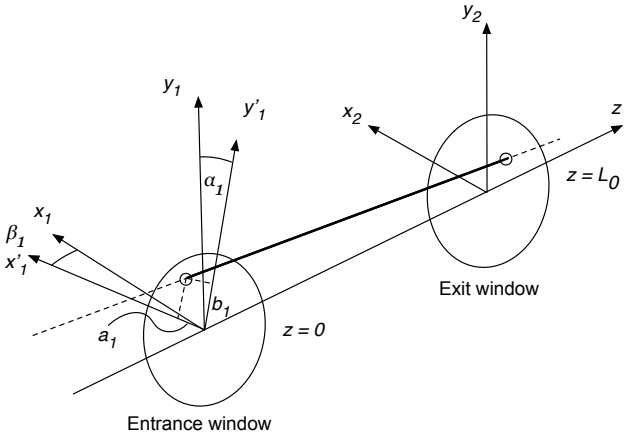

Figure A1. Geometry for the calculation of the absorption length. Two arbitrarily oriented spherical windows are located at a distance L_0 along the z axis. Unprimed axes designate coordinates in the laboratory frame, and primed axes apply to coordinates on the window surfaces. Euler angles α_1, β_1 define the window orientation. The light beam, indicated by a bold line between the windows, passes through the entrance window at point $(x_1',\ y_1') = (a_1, b_1)$ on the outer surface. The window thickness is ignored in the drawing.

takes into account any beam inclination with respect to the z axis. We note in passing that $L_0 = \mathcal{L}\sec\alpha$ for parallel windows and that in this case, $l_p^{(0)}$ is just the difference between the outer window distance and twice the effective window thickness.

When, as in our setup, windows are slightly non-parallel ($\Delta\alpha \ll 1$, $\Delta\beta \ll 1$) the single path length might conveniently be expressed as a linear expansion in the non-parallelism parameters. Thus for first-order terms, the length may be expressed as

$$l = l^{(0)} + l_{\Delta\alpha}^{(1)}\Delta\alpha + l_{\Delta\beta}^{(1)}\Delta\beta + \mathcal{O}(\Delta\alpha^k\Delta\beta^m), \quad k, m \ge 0 \wedge k + m = 2. \tag{A4}$$

As a matter of fact, the agreement between this approximation and the exact solution is better than 2 nm for a single pass in our configuration. For extreme conditions with $\alpha = 5°$, $\beta = 0$ or $\alpha = 0$, $\beta = 5°$ and $\Delta\alpha$ and $\Delta\beta$ in the 0.5° range, where the beam passes through the 30 cm cell within 5 mm of the centre, we find that the linear approximation for one pass always agrees with the full analytic solution by better than 12 µm, which is close to the calliper resolution. Let us introduce some quantities for deriving the coefficients in Eq. (A4):

$$\overline{x} = x + \Delta x/2, \quad \overline{y} = y + \Delta y/2, \quad \Delta = \sqrt{\Delta x^2 + \Delta y^2} \tag{A5}$$

$$\mathcal{B} = 3\sin\alpha + \sin 3\alpha - 4\frac{R+\overline{y}}{\mathcal{L}}\cos\alpha. \tag{A6}$$

Here, the average horizontal $\overline{x}$ and vertical $\overline{y}$ beam displacements are introduced. Using these abbreviations and the definition of $\mathcal{A}$ in Eq. (A3), the partial derivatives for the first-order corrections in $\Delta\beta$ and $\Delta\alpha$ are given as

$$\begin{aligned} l^{(1)}_{\Delta\alpha} = &\frac{\mathcal{L}}{2\mathcal{A}}\left\{\mathcal{B}\left[\left(1+\frac{2d}{\mathcal{L}\cos\beta}\right)\left(\frac{\Delta x}{\mathcal{L}}\sin\beta\frac{\Delta y}{\mathcal{L}}\tan\alpha\right)\right.\right. \\ &\left. - \frac{1}{\cos^2\alpha} - \frac{2d}{\mathcal{L}\cos\beta}\left(\frac{\Delta}{\mathcal{L}}\right)^2\right] + 4\cos\alpha\left(1-\frac{2d}{\mathcal{L}\cos\beta}\right) \\ &\left.\times\left(\frac{\Delta y}{\mathcal{L}}-\tan\alpha\right)\left(\frac{\overline{x}}{\mathcal{L}}\sin\beta+\frac{\overline{y}}{\mathcal{L}}\tan\alpha\right)\right\}, \end{aligned} \tag{A7}$$

$$l^{(1)}_{\Delta\beta} = \frac{2\overline{x}\cos\alpha}{\mathcal{A}}\left\{\cos\beta - \frac{2d}{\mathcal{L}}\left[1-\left(\frac{\mathcal{A}}{\cos\alpha\cos\beta}\right)^2\right]\right\}. \tag{A8}$$

Appendix B: Correlation terms

The correlation coefficients $r_{ij} = u^2(x_i, x_j)/(u(x_i)u(x_j))$ can be obtained from a generalised uncertainty propagation rule:

$$\begin{aligned} u^2(x_i(y), x_j(y)) = &\sum_{k=1}^{n}\sum_{r=1}^{m}\left(\frac{\partial x_i}{\partial y_{k,r}}\right)\left(\frac{\partial x_j}{\partial y_{k,r}}\right)u^2(y_{k,r}) \\ &+ \sum_{\substack{l,k=1\\ l\neq k}}^{n}\sum_{\substack{s,r=1\\ s\neq r}}^{m}\left(\frac{\partial x_i}{\partial y_{k,r}}\right)\left(\frac{\partial x_j}{\partial y_{l,s}}\right)u^2(y_{k,r}, y_{l,s}). \end{aligned} \tag{B1}$$

Summation indices (k,l) and (r,s) respectively go over the number n of observables y in Eq. (8) and the number m of different measurements. By setting $i = j$ and identifying covariance terms $u^2(x_i, x_i)$ by variances $u^2(x_i)$, we recover the familiar propagation rule for standard uncertainties with contributions from both variance and covariance terms. Equation (B1) considerably simplifies when cross-correlation terms vanish. In our case, variables k_B, ν_c, L, c_T and T_0 are common to all realisations and stochastically independent of all other quantities. Their covariance terms thus disappear completely. Due to temperature (T), pressure (p) and residual gas (ν_nc) measurements being independent of each other, covariances between T and p, between T and ν_nc and between p and ν_nc also mutually vanish, and so do the variance terms of these variables, because their sensitivity coefficients are necessarily 0 for $i \neq j$. One thus finds

$$\begin{aligned} \frac{u^2(x_i, x_j)}{x_i x_j} = &u_\mathrm{r}^2(k_\mathrm{B}) + u_\mathrm{r}^2(L) \\ &+ \frac{(T_i - T_0)(T_j - T_0)u^2(c_T)}{(1 - c_T(T_i - T_0))(1 - c_T(T_j - T_0))} \\ &+ \frac{u^2(\nu_\mathrm{c}) + u^2(\nu_{\mathrm{nc},i}, \nu_{\mathrm{nc},j})}{(1 - \nu_\mathrm{c} - \nu_{\mathrm{nc},i})(1 - \nu_\mathrm{c} - \nu_{\mathrm{nc},j})} + \frac{u^2(p_i, p_j)}{p_i p_j} \\ &+ \frac{(1 - c_T T_0)^2}{(1 - c_T(T_i - T_0))(1 - c_T(T_j - T_0))}\frac{u^2(T_i, T_j)}{T_i T_j}. \end{aligned} \tag{10}$$

Note that $u(T_0) = 0$ due to T_0 being an arbitrary constant and that we have introduced the normalisation factor $x_i x_j$, which expresses the covariances on the same footing as (the squared) relative uncertainties.

Author contributions. CJ and HE designed and performed the experiments. CJ analysed and interpreted the data. CJ and JG wrote the paper.

Competing interests. The authors declare that they have no conflict of interest.

Acknowledgements. We thank the entire technical staff at LERMA and the glass blowers Jean Pierre Francois from LPMAA and Florence Thibout from LKB, without whom the work could not have been realised. Christof Janssen also would like to thank Matthew Spidell and Gillian Nave from NIST for extended discussions, in which they openly shared their expertise on HeCd lasers and atomic emission lines. The work received funding from the French national programme LEFE/INSU. Julian Gröbner received financial support from the European Metrology Research Programme (EMRP) within the joint research project EMRP ENV59 ATMOZ "Traceability for atmospheric total column ozone". The EMRP is jointly funded by the EMRP participating countries within EURAMET and the European Union.

Edited by: Mark Weber
Reviewed by: two anonymous referees

References

Amiri-Simkooei, A. R., Zangeneh-Nejad, F., Asgari, J., and Jazaeri, S.: Estimation of straight line parameters with fully correlated coordinates, Measurement, 48, 378–386, 2014.

Barbe, A., Mikhailenko, S., Starikova, E., De Backer, M.-R., Tyuterev, V. G., Mondelain, D., Kassi, S., Campargue, A., Janssen, C., Tashkun, S., Kochanov, R., Gamache, R., and Orphal, J.: Ozone spectroscopy in the electronic ground state: high-resolution spectra analyses and update of line parameters since 2003, J. Quant. Spectrosc. Ra., 130, 172–190, 2013.

Bass, A. M. and Paur, R. J.: The ultraviolet cross-sections of ozone: I. The measurements, Atmospheric Ozone, edited by: Zerefos, C., and Ghazi, A., Reidel Publ. Co., Dordrecht, 606–610, 1985.

Bremser, W. and Hässelbarth, W.: Shall we consider covariances?, Accredit. Qual. Assur., 3, 106–110, 1998.

Bremser, W., Viallon, J., and Wielgosz, R. I.: Influence of correlation on the assessment of measurement result compatibility over a dynamic range, Metrologia, 44, 495–504, 2007.

Brion, J., Chakir, A., Daumont, D., Malicet, J., and Parisse, C.: High-resolution laboratory absorption cross section of O_3 – temperature effect, Chem. Phys. Lett., 213, 610–612, 1993.

Burns, K. and Adams, K. B.: Energy levels and wavelengths of natural cadmium and of cadmium-114, J. Opt. Soc. Am., 46, 94–99, 1956.

Cantrell, C. A.: Technical Note: Review of methods for linear least-squares fitting of data and application to atmospheric chemistry problems, Atmos. Chem. Phys., 8, 5477–5487, https://doi.org/10.5194/acp-8-5477-2008, 2008.

Ciddor, P. E.: Refractive index of air: new equations for the visible and near infrared, Appl. Optics, 35, 1566–1573, 1996.

Cuesta, J., Eremenko, M., Liu, X., Dufour, G., Cai, Z., Höpfner, M., von Clarmann, T., Sellitto, P., Foret, G., Gaubert, B., Beekmann, M., Orphal, J., Chance, K., Spurr, R., and Flaud, J.-M.: Satellite observation of lowermost tropospheric ozone by multispectral synergism of IASI thermal infrared and GOME-2 ultraviolet measurements over Europe, Atmos. Chem. Phys., 13, 9675–9693, https://doi.org/10.5194/acp-13-9675-2013, 2013.

Daudé, B., Elandaloussi, H., and Janssen, C.: On the gas dependence of thermal transpiration and a critical appraisal of correction methods for capacitive diaphragm gauges, Vacuum, 104, 77–87, 2014.

Daumont, D., Brion, J., Charbonnier, J., and Malicet, J.: Ozone UV spectroscopy. 1. Absorption cross sections at room temperature, J. Atmos. Chem., 15, 145–155, 1992.

Deming, W. E.: Statistical Adjustment of Data, Wiley, NY, Dover Publications (1985) Edn., 1943.

Flaud, J. M., Wagner, G., Birk, M., Camy-Peyret, C., Claveau, C., DeBacker-Barilly, M. R., Barbe, A., and Piccolo, C.: Ozone absorption around 10 µm, J. Geophys. Res., 108, 4269, https://doi.org/10.1029/2002JD002755, 2003.

Gorshelev, V., Serdyuchenko, A., Weber, M., Chehade, W., and Burrows, J. P.: High spectral resolution ozone absorption cross-sections – Part 1: Measurements, data analysis and comparison with previous measurements around 293 K, Atmos. Meas. Tech., 7, 609–624, https://doi.org/10.5194/amt-7-609-2014, 2014.

Gratien, A., Picquet-Varrault, B., Orphal, J., Doussin, J. F., and Flaud, J. M.: New laboratory intercomparison of the ozone absorption coefficients in the mid-infrared (10 µm) and ultraviolet (300–350 nm) spectral regions, J. Phys. Chem. A, 114, 10045–10048, 2010.

Guinet, M., Mondelain, D., Janssen, C., and Camy-Peyret, C.: Laser spectroscopic study of ozone in the 100←000 band for the SWIFT instrument, J. Quant. Spectrosc. Ra., 111, 961–972, 2010.

Haynes, W. M. (Ed.): CRC Handbook of Chemistry and Physics, CRC Press, Taylor & Francis Group, Boca Raton, FL, 96th (2015–2016) Edn., 2015.

Hearn, A. G.: The absorption of ozone in the ultra-violet and visible regions of the spectrum, Proc. Phys. Soc., 78, 932–940, 1961.

ISO: Determination and use of straight-line calibration functions, Technical Specification ISO/TS 28037:2010(E), International Organization for Standardization (ISO), 2010.

Janssen, C., Simone, D., and Guinet, M.: Preparation and accurate measurement of pure ozone, Rev. Sci. Instrum., 82, 034102, https://doi.org/10.1063/1.3557512, 2011.

Janssen, C., Boursier, C., Jeseck, P., and Té, Y.: Line parameter study of ozone at 5 and 10 µm using atmospheric FTIR spectra from the ground: A spectroscopic database and wavelength region comparison, J. Mol. Spectrosc., 326, 48–59, 2016.

Kagawa, A., Kasai, Y., Jones, N. B., Yamamori, M., Seki, K., Murcray, F., Murayama, Y., Mizutani, K., and Itabe, T.: Characteristics and error estimation of stratospheric ozone and ozone-related species over Poker Flat (65° N, 147° W), Alaska observed by a ground-based FTIR spectrometer from 2001 to 2003, Atmos. Chem. Phys., 7, 3791–3810, https://doi.org/10.5194/acp-7-3791-2007, 2007.

Lakkala, K., Arola, A., Heikkilä, A., Kaurola, J., Koskela, T., Kyrö, E., Lindfors, A., Meinander, O., Tanskanen, A., Gröbner, J., and Hülsen, G.: Quality assurance of the Brewer spectral UV

measurements in Finland, Atmos. Chem. Phys., 8, 3369–3383, https://doi.org/10.5194/acp-8-3369-2008, 2008.

Lantz, K., Disterhoft, P., Early, E., Thompson, A., DeLuisi, J., Berndt, J., Harrison, L., Kiedron, P., Ehramjian, J., Bernhard, G., Cabasug, L., Robertson, J., Mou, W., Taylor, T., Slusser, J., Bigelow, D., Durham, B., Janson, G., Hayes, D., Beaubien, M., and Beaubien, A.: The 1997 North American Interagency Intercomparison of Ultraviolet Spectroradiometers Including Narrowband Filter Radiometers, J. Res. Natl. Inst. Stan., 107, 19–62, 2002.

Ludwig, K. R. and Titterington, D. M.: Calculation of ^{230}Th/U isochrons, ages, and errors, Geochim. Cosmochim. Ac., 58, 5031–5042, 1994.

Malengo, A. and Pennecchi, F.: A weighted total least-squares algorithm for any fitting model with correlated variables, Metrologia, 50, 654–662, 2013.

Malicet, J., Brion, J., and Daumont, D.: New values of ozone absolute cross-sections in the ultra violet spectral range at 298 and 228 K, by a method based upon pressure measurements at constant volume, in: Atmospheric Ozone, edited by: Zerefos, C., and Ghazi, A., Reidel Publ. Co., Dordrecht, 617–621, 1985.

Malicet, J., Daumont, D., Charbonnier, J., Parisse, C., Chakir, A., and Brion, J.: Ozone UV spectroscopy. 2. Absorption cross sections and temperature dependence, J. Atmos. Chem., 21, 263–273, 1995.

Mielenz, K. D., Nefflen, K. F., Rowley, W. R., Wilson, D. C., and Engelhard, E.: Reproducibility of helium-neon laser wavelengths at 633 nm, Appl. Optics, 7, 289–293, 1968.

Orphal, J.: A critical review of the absorption cross-sections of O_3 and NO_2 in the ultraviolet and visible, J. Photoch. Photobio. A, 157, 33–31, 2003.

Orphal, J., Staehelin, J., Tamminen, J., Braathen, G., De Backer, M. R., Bais, A. F., Balis, D., Barbe, A., Bhartia, P. K., Birk, M., Burkholder, J. B., Chance, K. V., von Clarman, T., Cox, A., Degenstein, D., Evans, R., Flaud, J. M., Flittner, D., Godin-Beckmann, S., Gorshelev, V., Hare, E., Janssen, C., Kyrölä, E., Mcelroy, T., McPeters, R., Pastel, M., Petersen, M., Petropavlovskikh, I., Picquet-Varrault, B., Pitts, M., Labow, G., Rotger-Langerau, M., Leblanc, T., Lerot, C., Liu, X., Moussay, P., Redondas, A., Van Roozendael, M., Sander, S. P., Schneider, M., Serdyuchenko, A., Veefkind, P., Viallon, J., Viatte, C., Wagner, G., Weber, M., Wielgosz, R. I., and Zahner, C.: Absorption cross-sections of ozone in the ultraviolet and visible spectral regions – Status report 2015, J. Mol. Spectrosc., 327, 105–121, 2016.

Paur, R. J. and Bass, A. M.: The ultraviolet cross-sections of ozone: II. Results and temperature dependence, in: Atmospheric Ozone, edited by: Zerefos, C. and Ghazi, A., Reidel Publ. Co., Dordrecht, 611–616, 1985.

Picquet-Varrault, B., Orphal, J., Doussin, J.-F., Carlier, P., and Flaud, J.-M.: Intercomparison of the ozone absorption coefficients in the mid-infrared (10 µm) and ultraviolet (300–350 nm) spectral regions, J. Phys. Chem. A, 109, 1008–1014, 2005.

Platt, U. and Perner, D.: An Instrument for the Spectroscopic Measurement of Trace Substances in the Atmosphere, Fresen. Z. Anal. Chem., 317, 309–313, 1984.

Reader, J., Corliss, C. H., Wiese, W. L., and Martin, G. A.: Wavelengths and transition probabilities for atoms and atomic ions: Part I. Wavelengths, Tech. Rep. NSRDS-NBS 68, National Bureau of Standards, Gaithersburg, MD, 1980.

Reed, B. C.: Straight-line fits with uncertainties in both coordinates: from Gauss to spreadsheets, Phys. Scripta, 90, 1–13, 2015.

Rothman, L. S., Jacquemart, D., Barbe, A., Benner, D. C., Birk, M., Brown, L. R., Carleer, M. R., Chackerian, Jr, C., Chance, K., Coudert, L. H., Dana, V., Devi, V. M., Flaud, J.-M., Gamache, R. R., Goldman, A., Hartmann, J.-M., Jucks, K. W., Maki, A. G., Mandin, J.-Y., Massie, S. T., Orphal, J., Perrin, A., Rinsland, C. P., Smith, M. A. H., Tennyson, J., Tolchenov, R. N., Toth, R. A., Vander Auwera, J., Varanasi, P., and Wagner, G.: The HITRAN 2004 Molecular Spectroscopic Database, J. Quant. Spectrosc. Ra., 96, 139–204, 2005.

Rothman, L. S., Gordon, I. E., Babikov, Y., Barbe, A., Chris Benner, D., Bernath, P. F., Birk, M., Bizzocchi, L., Boudon, V., Brown, L. R., Campargue, A., Chance, K., Cohen, E. A., Coudert, L. H., Devi, V. M., Drouin, B. J., Fayt, A., Flaud, J. M., Gamache, R. R., Harrison, J. J., Hartmann, J. M., Hill, C., Hodges, J. T., Jacquemart, D., Jolly, A., Lamouroux, J., Le Roy, R. J., Li, G., Long, D. A., Lyulin, O. M., Mackie, C. J., Massie, S. T., Mikhailenko, S., Müller, H. S. P., Naumenko, O. V., Nikitin, A. V., Orphal, J., Perevalov, V., Perrin, A., Polovtseva, E. R., Richard, C., Smith, M. A. H., Starikova, E., Sung, K., Tashkun, S., Tennyson, J., Toon, G. C., Tyuterev, V. G., and Wagner, G.: The HITRAN2012 molecular spectroscopic database, J. Quant. Spectrosc. Ra., 130, 4–50, 2013.

Sansonetti, J. E. and Martin, W. C.: Handbook of basic atomic spectroscopic data, J. Phys. Chem. Ref. Data, 34, 1559–1702, 2005.

Serdyuchenko, A., Gorshelev, V., Weber, M., Chehade, W., and Burrows, J. P.: High spectral resolution ozone absorption cross-sections – Part 2: Temperature dependence, Atmos. Meas. Tech., 7, 625–636, https://doi.org/10.5194/amt-7-625-2014, 2014.

Shenstone, A. G. and Pittenger, J. T.: Cadmium Spectra, J. Opt. Soc. Am., 39, 219–225, 1949.

Viallon, J., Moussay, P., Norris, J. E., Guenther, F. R., and Wielgosz, R. I.: A study of systematic biases and measurement uncertainties in ozone mole fraction measurements with the NIST Standard Reference Photometer, Metrologia, 43, 441–450, 2006.

Viallon, J., Lee, S., Moussay, P., Tworek, K., Petersen, M., and Wielgosz, R. I.: Accurate measurements of ozone absorption cross-sections in the Hartley band, Atmos. Meas. Tech., 8, 1245–1257, https://doi.org/10.5194/amt-8-1245-2015, 2015.

Viatte, C., Schneider, M., Redondas, A., Hase, F., Eremenko, M., Chelin, P., Flaud, J.-M., Blumenstock, T., and Orphal, J.: Comparison of ground-based FTIR and Brewer O_3 total column with data from two different IASI algorithms and from OMI and GOME-2 satellite instruments, Atmos. Meas. Tech., 4, 535–546, https://doi.org/10.5194/amt-4-535-2011, 2011.

Voigt, S., Orphal, J., Bogumil, K., and Burrows, J. P.: The temperature dependence (203–293 K) of the absorption cross sections of O_3 in the 230–850 nm region measured by Fourier-transform spectroscopy, J. Photoch. Photobio. A, 143, 1–9, 2001.

Weber, M., Gorshelev, V., and Serdyuchenko, A.: Uncertainty budgets of major ozone absorption cross sections used in UV remote sensing applications, Atmos. Meas. Tech., 9, 4459–4470, https://doi.org/10.5194/amt-9-4459-2016, 2016.

Wehr, R. and Saleska, S. R.: The long-solved problem of the best-fit straight line: application to isotopic mixing lines, Bio-

geosciences, 14, 17–29, https://doi.org/10.5194/bg-14-17-2017, 2017.

Williamson, J. H.: Least-squares fitting of a straight line, Can. J. Phys., 46, 1845–1847, 1968.

Wolfram Research, Inc.: Mathematica, 2016.

York, D.: Least-squares fitting of a straight line, Can. J. Phys., 44, 1079–1086, 1966.

York, D.: Least squares fitting of a straight line with correlated errors, Earth Planet. Sc. Lett., 5, 320–324, 1968.

York, D., Evensen, N. M., López Martínez, M., and De Basabe Delgado, J.: Unified equations for the slope, intercept, and standard errors of the best straight line, Am. J. Phys., 72, 367–375, 2004.